AIAA JOURNAL
Vol. 31, No. 8, August 1993

Large-Eddy Simulation of Turbulent Obstacle Flow Using a Dynamic Subgrid-Scale Model

Kyung-Soo Yang* and Joel H. Ferziger†
Stanford University, Stanford, California 94305

We apply the dynamic subgrid-scale model to a large-eddy simulation of turbulent channel flow with a square rib mounted on one wall. The Reynolds number Re is 3.21×10^3 based on the mean velocity above the obstacle and the obstacle's height. Near-wall structures are resolved with the no-slip boundary condition. The results show better agreement with direct numerical simulation than large-eddy simulation with a fixed model constant, verifying the value of the dynamic subgrid-scale model for simulating complex turbulent flows.

I. Introduction

LARGE-EDDY simulation (LES) is an accurate method of simulating complex turbulent flows in which the large flow structures are computed while small scales are modeled. The rationale behind this method is based on two observations: most of the turbulent energy is in the large structures, and the small scales are more isotropic and universal. Therefore, LES may be more general and less geometry dependent than Reynolds-averaged modeling, although it comes at higher cost.

Even though LES has been used by many investigators, most research has been limited to flows with simple geometry. In engineering applications, however, one encounters more complicated geometries. Here we shall consider a rectangular parallelepiped mounted on a flat surface. Related flows are those over surfaces protruding from submarines (conning towers or control fins), wind flows around buildings, and airflows over computer chips, among others. The most distinctive features associated with these flows are three dimensionality, flow separation due to protruding surfaces, and large-scale unsteadiness. As a model flow, we consider a plane channel flow in which a two-dimensional obstacle is mounted on one surface (see Fig. 1). This relatively simple geometry contains flow separation and reattachment. Flow in this geometry has been studied by Tropea and Gackstatter[1] for low Re and Werner and Wengle[2] and Dimaczek et al.[3] for high Re, among others.

Recently, Germano et al.[4] suggested a dynamic subgrid-scale model (DSGSM) in which the model coefficient is dynamically computed as computation progresses rather than specified a priori. This approach is based on an algebraic identity between the subgrid-scale stresses at two different filter levels and the resolved turbulent stresses. They applied the model to transitional and fully turbulent channel flows and showed that the model contributes nothing in laminar flow and exhibits the correct asymptotic behavior in the near-wall region of turbulent flows without an ad hoc damping function. This is a significant improvement over conventional subgrid-scale modeling.

In complex geometries, however, it is more difficult to use the dynamic model owing to the lack of homogeneous directions in which to do spatial averaging of the model coefficient. In this paper, we perform an LES of turbulent flow in a channel containing a two-dimensional obstacle on one wall using a DSGSM at $Re = 3.2 \times 10^3$, based on bulk velocity above the obstacle U_m and obstacle height h; the wall layers are fully resolved. The low Re enables us to perform a direct numerical simulation (DNS) (case I) against which to validate the LES results. The LES with the DSGSM is designated case II. In addition, an LES with the conventional fixed model constant (case III) is conducted to allow identification of improvements due to the DSGSM.

II. Formulation

All variables are nondimensionalized by U_m and h. The code uses a nonuniform Cartesian staggered grid in a finite volume approach. The incompressible momentum equations filtered by a simple volume-average box filter are

$$\frac{\partial \bar{u}_i}{\partial t} + \frac{\partial}{\partial x_j}(\overline{u_i u_j}) = -\frac{\partial \bar{p}}{\partial x_i} + \frac{1}{Re}\frac{\partial^2 \bar{u}_i}{\partial x_j \partial x_j} \tag{1}$$

where u_1, u_2, and u_3 (or u, v, and w) are velocities in x_1 (streamwise), x_2 (normal), and x_3 (spanwise) directions (or x, y, and z), respectively, and p is pressure. The volume-average box filter is defined by

$$\bar{u}_i(x_1,x_2,x_3,t) = \frac{1}{\Delta x_1 \Delta x_2 \Delta x_3}\int\int\int u_i(x_1',x_2',x_3',t)\,dx_1'\,dx_2'\,dx_3' \tag{2}$$

where the integrations are performed on a control volume. The convective term can be rewritten as

$$\frac{\partial}{\partial x_j}(\overline{u_i u_j}) = \frac{\partial}{\partial x_j}(\bar{u}_i \bar{u}_j + L_{ij} + C_{ij} + R_{ij}) \tag{3}$$

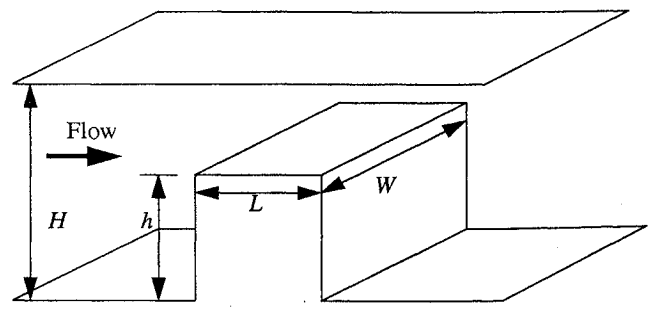

Fig. 1 Physical configuration.

Received Oct. 3, 1992; presented as Paper 93-0542 at the AIAA 31st Aerospace Sciences Meeting, Reno, NV, Jan. 11-14, 1993; revision received Jan. 12, 1993; accepted for publication Jan. 13, 1993.

*Research Associate, Department of Mechanical Engineering; currently Assistant Professor, Department of Mechanical Engineering, Inha University, Inchon 402-751, Korea.

†Professor, Department of Mechanical Engineering. Member AIAA.

where

$$L_{ij} = \overline{\bar{u}_i \bar{u}_j} - \bar{u}_i \bar{u}_j$$
$$C_{ij} = \overline{\bar{u}_i u'_j} + \overline{\bar{u}_j u'_i} \tag{4}$$
$$R_{ij} = \overline{u'_i u'_j}$$

where L_{ij}, C_{ij}, and R_{ij} represent Leonard stresses, cross terms, and subgrid-scale Reynolds stresses, respectively. When a finite difference scheme of second-order accuracy is used, the Leonard stresses are of the same order as the truncation error (Shaanan et al.[5]). The other terms have to be modeled.

The governing equations for LES become

$$\frac{\partial \bar{u}_i}{\partial x_i} = 0 \tag{5}$$

$$\frac{\partial \bar{u}_i}{\partial t} + \frac{\partial}{\partial x_j}(\bar{u}_i \bar{u}_j) = -\frac{\partial P}{\partial x_i} + \frac{1}{Re}\frac{\partial^2 \bar{u}_i}{\partial x_j \partial x_j} - \frac{\partial \tau_{ij}}{\partial x_j} \tag{6}$$

where

$$\tau_{ij} = Q_{ij} - \tfrac{1}{3} Q_{kk} \delta_{ij}$$
$$P = \bar{p} + \tfrac{1}{3} Q_{kk} \tag{7}$$
$$Q_{ij} = R_{ij} + C_{ij}$$

where δ_{ij} is the Kronecker symbol. In the present simulation, the eddy viscosity model of Smagorinsky[6] is used:

$$\tau_{ij} = -2\nu_T \bar{S}_{ij} \tag{8}$$

where

$$\bar{S}_{ij} = \frac{1}{2}\left(\frac{\partial \bar{u}_i}{\partial x_j} + \frac{\partial \bar{u}_j}{\partial x_i}\right)$$
$$\nu_T = l^2 \sqrt{2 \bar{S}_{ij} \bar{S}_{ij}} \tag{9}$$

where l is a characteristic length scale of the small eddies. In case III, the smaller value of κd and $0.1\,\bar{\Delta}$ is used for l, where κ and d are von Kármán's constant and the distance normal to a wall, respectively, and $\bar{\Delta} = (\Delta x \Delta y \Delta z)^{1/3}$. The particular form of τ_{ij} in Eq. (7) is chosen to make both (7) and (8) consistent on contraction ($i = j$).

In case II, l^2 is dynamically determined as follows. Let

$$t_{ij} = \overline{\bar{u}_i \bar{u}_j} - \bar{u}_i \bar{u}_j \tag{10}$$

be the sum of the three terms in Eq. (4), i.e., the total term to be modeled. A test filter of larger width $\tilde{\bar{\Delta}}$ than the original filter width $\bar{\Delta}$ is introduced and denoted by a tilde. Applying the test filter to Eq. (1), one obtains a subgrid-scale stress similar to Eq. (10):

$$T_{ij} = \widetilde{\bar{u}_i \bar{u}_j} - \tilde{\bar{u}}_i \tilde{\bar{u}}_j \cdot \tag{11}$$

Let

$$D_{ij} = \widetilde{\bar{u}_i \bar{u}_j} - \tilde{\bar{u}}_i \tilde{\bar{u}}_j \cdot \tag{12}$$

Rearrangement of Eqs. (10–12) yields the algebraic relation

$$D_{ij} = T_{ij} - \tilde{t}_{ij} \tag{13}$$

Assuming that the same functional form and coefficient C_s can be used to model the anisotropic parts of both t_{ij} and T_{ij},

$$t_{ij} - \frac{\delta_{ij}}{3} \cdot t_{kk} \approx \tau_{ij} = -2C_s \bar{\Delta}^2 |\bar{S}| \bar{S}_{ij} \tag{14}$$

and

$$T_{ij} - \frac{\delta_{ij}}{3} \cdot T_{kk} \approx M_{ij} = -2C_s \tilde{\bar{\Delta}}^2 |\tilde{\bar{S}}| \tilde{\bar{S}}_{ij} \tag{15}$$

where

$$\tilde{\bar{S}}_{ij} = \frac{1}{2}\left(\frac{\partial \tilde{\bar{u}}_i}{\partial x_j} + \frac{\partial \tilde{\bar{u}}_j}{\partial x_i}\right), \qquad |\tilde{\bar{S}}| = \sqrt{2 \tilde{\bar{S}}_{ij} \tilde{\bar{S}}_{ij}} \tag{16}$$

where C_s is a coefficient to be computed ($l^2 = C_s \bar{\Delta}^2$). Substituting Eqs. (14) and (15) into Eq. (13) gives

$$D_{ij} - \frac{\delta_{ij}}{3} \cdot D_{kk} = 2C_s(\bar{\Delta}^2 |\tilde{\bar{S}}| \tilde{\bar{S}}_{ij} - \tilde{\bar{\Delta}}^2 |\tilde{\bar{S}}| \tilde{\bar{S}}_{ij}) = 2C_s P_{ij} \tag{17}$$

There are many ways to calculate C_s using Eq. (17). Lilly[7] suggested a least-squares approach that leads to

$$C_s = \frac{1}{2}\frac{D_{ij} P_{ij}}{P_{ij} P_{ij}} \tag{18}$$

This method yields a computationally more stable value of C_s than the method of Germano et al.[4] that is based on contracting Eq. (17) with $\tilde{\bar{S}}_{ij}$. In their approach, the denominator may vanish or become so small that C_s could be large enough to cause computational instability. In contrast, the denominator of Eq. (18) can vanish only if all nine components vanish at the same time; in that case, the numerator also vanishes. Both approaches allow negative values of C_s, which means that net "backscatter" is permitted.

Since C_s is an instantaneous and local quantity, it can vary wildly in time and space and may lead to numerical instability. To avoid this possibility, averaging is performed in space and time. Spatial averaging is done in the homogeneous z direction first. Then additional averaging is performed over nine neighboring grid points with the point for which the averaging is carried out at the center, using volume weighting, to obtain an averaged value of C_s at a given inner grid point. In the near-wall region, averaging is done only in the direction parallel to the solid wall, i.e., using three points. It is necessary to repeat this process to smooth C_s sufficiently. Germano et al.[4] found the optimum value of the ratio $\tilde{\bar{\Delta}}/\bar{\Delta}$ to be 2, a value we adopted.

III. Numerical Method

To advance the solution in time, a fractional step method (Kim and Moin[8]) is employed. The time advancement of the momentum equation is hybrid; the convective terms are explicitly advanced by a third-order Runge-Kutta scheme and the viscous terms implicitly by the Crank-Nicolson method:

$$\frac{\hat{u}_i^k - \bar{u}_i^{k-1}}{\Delta t} = (\alpha_k + \beta_k) L(\bar{u}_i^{k-1}) + \beta_k L(\hat{u}_i^k - \bar{u}_i^{k-1}) - \gamma_k N(\bar{u}_i^{k-1}) - \zeta_k N(\bar{u}_i^{k-2}) - (\alpha_k + \beta_k)\frac{\partial \bar{P}^{k-1}}{\partial x_i} \tag{19}$$

$$\frac{\bar{u}_i^k - \hat{u}_i^k}{\Delta t} = -\frac{\partial \bar{\phi}^k}{\partial x_i} \qquad k = (1, 2, 3) \tag{20}$$

where

$$\frac{\partial \bar{P}^k}{\partial x_i} = \frac{\partial \bar{P}^{k-1}}{\partial x_i} + \left(\frac{1}{\alpha_k + \beta_k} - \frac{\beta_k \Delta t}{\alpha_k + \beta_k} L\right)\frac{\partial \bar{\phi}^k}{\partial x_i}$$
$$L = \frac{1}{Re}\frac{\partial^2}{\partial x_j \partial x_j} + \frac{\partial}{\partial x_j}\nu_T(1 + \delta_{ij})\frac{\partial}{\partial x_j}$$
$$N(\bar{u}_i) = \frac{\partial}{\partial x_j}(\bar{u}_i \bar{u}_j) - \frac{\partial}{\partial x_j}\nu_T(1 - \delta_{ij})\frac{\partial \bar{u}_j}{\partial x_i}$$

with

$$\gamma_1 = \frac{8}{15}, \quad \gamma_2 = \frac{5}{12}, \quad \gamma_3 = \frac{3}{4}, \quad \zeta_1 = 0, \quad \zeta_2 = -\frac{17}{60}$$
$$\zeta_3 = -\frac{5}{12}, \quad \alpha_1 = \beta_1 = \frac{4}{15}, \quad \alpha_2 = \beta_2 = \frac{1}{15}, \quad \alpha_3 = \beta_3 = \frac{1}{6}$$
$$\sum_{k=1}^{3}(\alpha_k + \beta_k) = \sum_{k=1}^{3}(\gamma_k + \zeta_k) = 1$$

In the expressions for L and $N(\bar{u}_i)$, summation is performed on the index j only. The momentum equation is time advanced without implicit pressure terms and then projected onto a divergence-free space by introducing $\bar{\phi}$ that obeys a Poisson equation. The latter is solved by a multigrid method that is very flexible and more efficient than a number of competitors. For spatial discretization, second-order accurate central differencing was used. All terms in the model except the cross derivatives are treated implicitly in all three directions to avoid restrictions on time steps.The code is well vectorized; a speed of 150 million floating point operations per second (MFlops) has been achieved on a Cray Y-MP/832.

IV. Results and Discussion

A. Choice of Parameters and Boundary Conditions

The values of the geometric parameters in all three cases are $h/H = 0.5$, $W/h = 2$, and $L/h = 1$, where H, W, and L are channel height, spanwise width of the obstacle and channel, and the obstacle's streamwise length, respectively (see Fig. 1). The inlet and the outlet are located at $x = 0$ and 31, respectively, and the obstacle is placed between $x = 10$ and 11.

In cases II and III (case I), the center of the control volume adjacent to the wall was placed at $\Delta y = 0.0086$ (0.005) from horizontal walls except on the top of the obstacle where the nearest center was placed at $\Delta y = 0.0046$ (0.0036). On the vertical walls the first grid points are at $\Delta x = 0.0045$ (0.0033) from the left wall, and $\Delta x = 0.014$ (0.0045) from the right wall. The grid is densely packed around the obstacle and near the channel walls and geometrically stretched in the other regions. The number of control volumes is $112 \times 48 \times 40$ ($272 \times 64 \times 64$) in the x, y, and z directions, respectively. Grid refinement shows that the spatial resolution is adequate; using more control volumes shows improvement, but the difference is insignificant.

In all cases, periodic boundary conditions were employed in the homogeneous (z) direction; at the walls, no-slip boundary conditions were imposed. We also apply periodic boundary conditions in the x direction to avoid any uncertainty related to outflow boundary condition, which has been an area of controversy, and to assure a reasonable flow approaching the obstacle. Therefore, we are actually simulating an infinitely long channel flow with a periodic array of obstacles. To minimize the interaction between "neighboring" obstacles, a long streamwise computational domain ($31h$) is employed.

Since the pressure difference between the inlet and the outlet is fixed, Re is slightly different in each case. To match the Reynolds numbers of the various cases as closely as possible, we adjusted the pressure difference slightly. The second column of Table 1 shows Re for each case. The 3% variation in Re should be kept in mind in the following comparisons.

After an initial transient period, the flow becomes fully turbulent and sustained. Then an averaging is performed in the homogeneous direction and in time to obtain averaged quantities. The time averaging was taken over 27 characteristic time units (h/U_m).

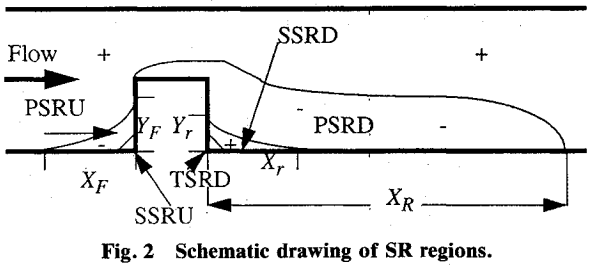

Fig. 2 Schematic drawing of SR regions.

Table 1 Comparison of various SR lengths

Case	Re	X_R	X_r	Y_r	X_F	Y_F
I	3.31×10^3	6.42	1.21	0.35	1.51	0.28
II	3.21×10^3	6.80	1.13	0.36	1.51	0.37
III	3.33×10^3	7.01	1.76	0.28	1.35	0.40

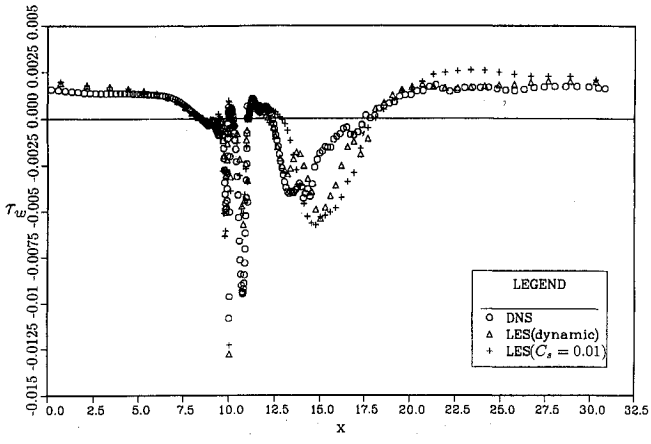

Fig. 3a Averaged wall shear stress at the lower wall.

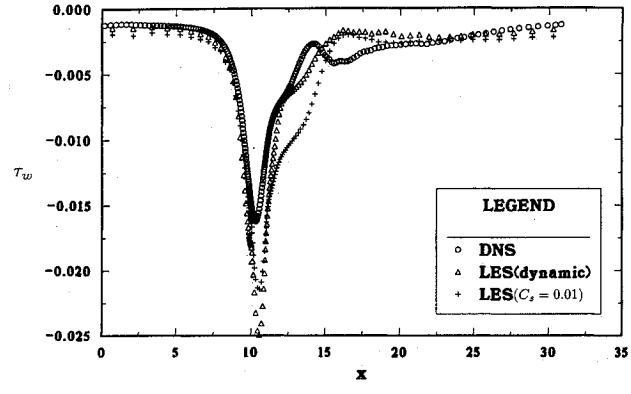

Fig. 3b Averaged wall shear stress at the upper wall.

B. Averaged Flowfield

The flow develops several separation and reattachment (SR) zones near the obstacle. Figure 2 shows schematic contours of $U = 0$ (U and V represent averaged values of u and v, respectively). The + and − signs indicate regions of positive and negative U, respectively. In addition to the primary SR zones upstream (PSRU) and downstream (PSRD) of the obstacle, there are secondary SR zones upstream (SSRU, at the front corner) and downstream (SSRD, near the rear corner, bigger than SSRU) of the obstacle. A tertiary SR zone is discernible at the downstream corner of the obstacle (TSRD). For the given geometry and Re, reattachment does not occur on top of the obstacle in any of the three cases. The reattachment length of PSRD is denoted by X_R. The separation length and reattachment length of PSRU are represented by X_F and Y_F, respectively, and those of SSRD by X_r and Y_r, respectively. Table 1 gives computed values of those lengths in units of h for each case. Case I, the DNS, is the most accurate simulation. Its X_R is consistent with the experiment of Tropea and Gackstatter[1]; they did not report the other SR lengths. Case II is significantly more accurate than case III for every length scale.

Figure 3 presents nondimensionalized shear stress (τ_w) on the lower (Fig. 3a) and upper walls (Fig. 3b). In Fig. 3a, the values of τ_w between $x = 10$ and 11 are for the top surface of the obstacle. The large differences in the values of τ_w on the top of the obstacle reflect the complexity of the flow in that region. The τ_w predicted by case II agrees better with case I in PSRD than does case III, especially for $11 \le x \le 13$ and far downstream ($x \ge 20$). Case II also gives better results on the upper channel wall (Fig. 3b). The large $|\tau_w|$ near $x = 10$ is caused by flow acceleration due to the sudden contraction in

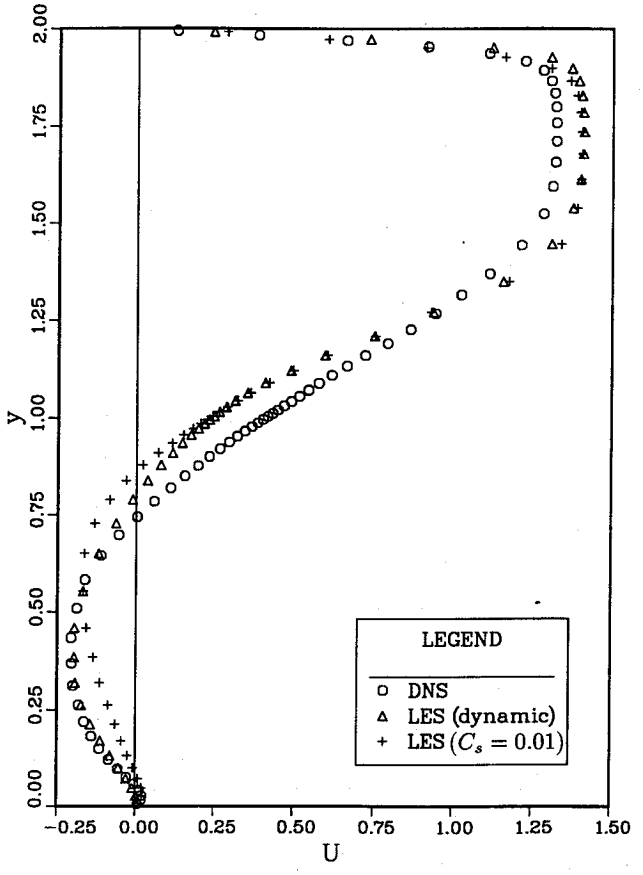

Fig. 4a Averaged streamwise velocity U profiles at $x = 12$.

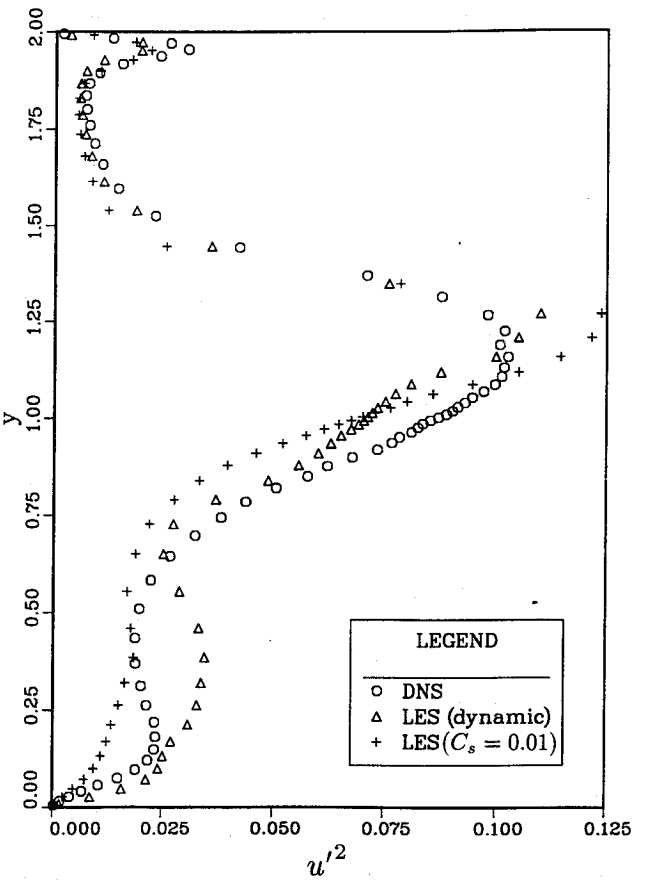

Fig. 5a Averaged streamwise turbulent fluctuation u'^2 profiles at $x = 12$.

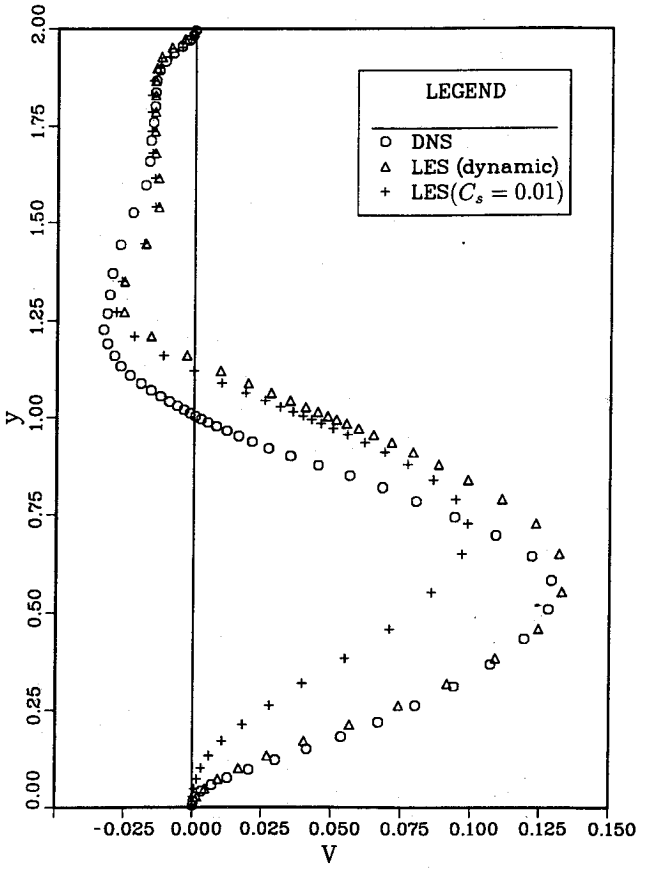

Fig. 4b Averaged normal velocity V profiles at $x = 12$.

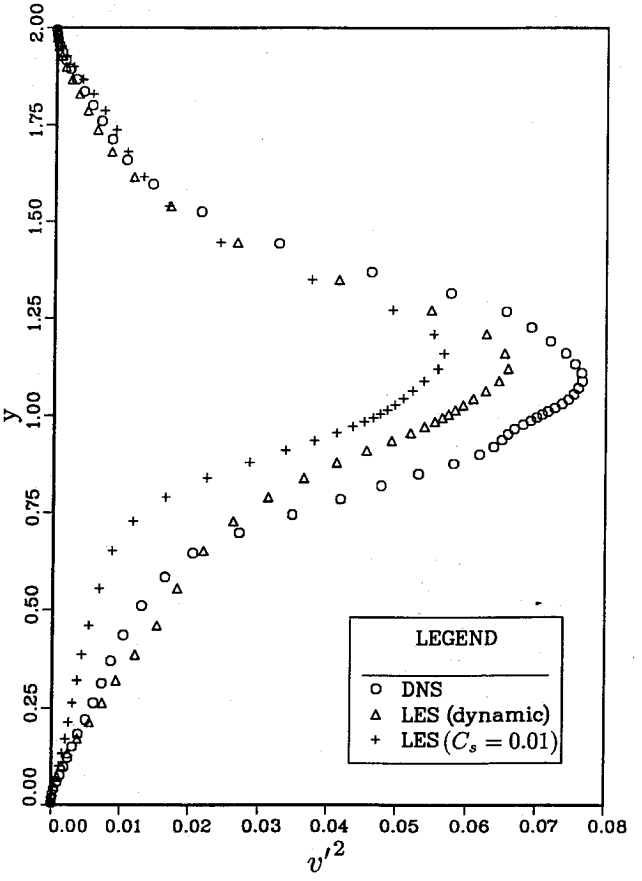

Fig. 5b Averaged normal turbulent fluctuation v'^2 profiles at $x = 12$.

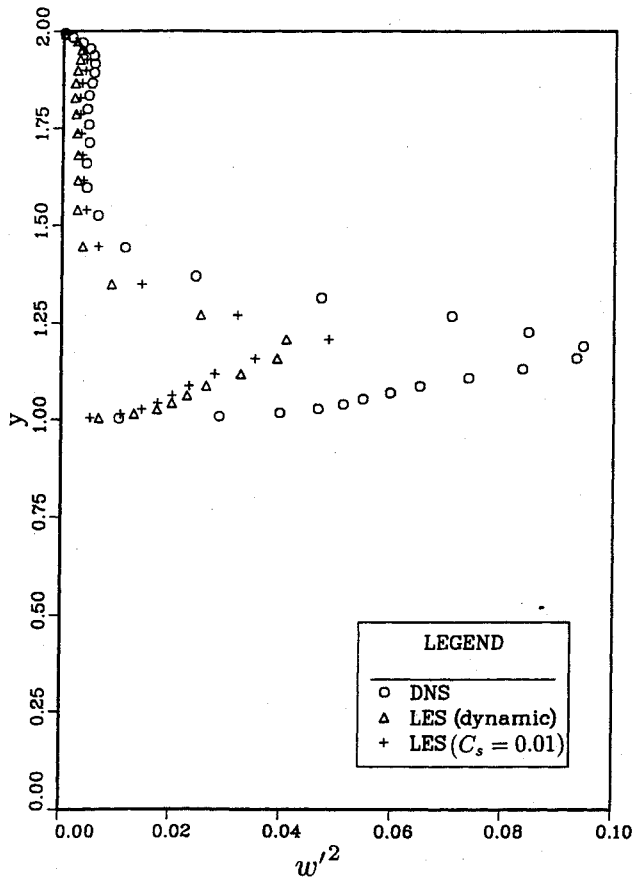

Fig. 5c Averaged spanwise turbulent fluctuation w'^2 profiles at $x = 11$.

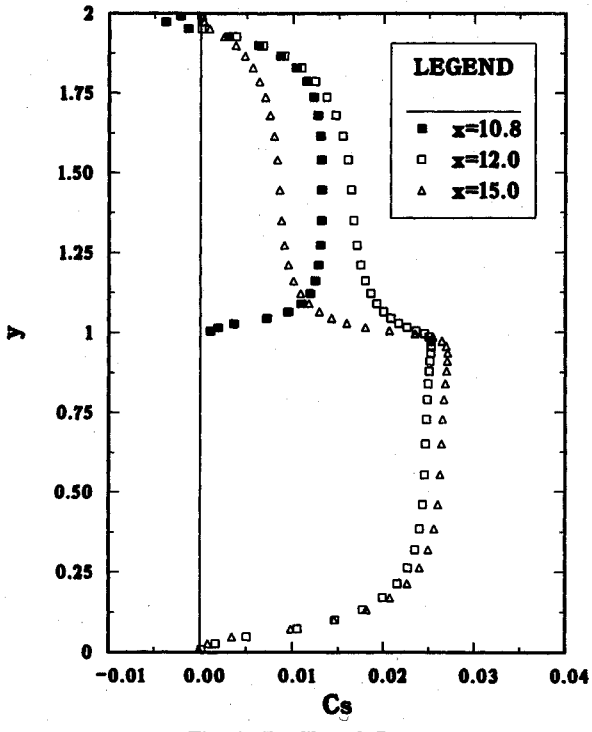

Fig. 6 Profiles of C_s.

flow passage. Better agreement for $11 \leq x \leq 15$ and in the "channel region" ($x \leq 7.5$ or ≥ 25) are also noticeable.

Profiles of U and V at a selected streamwise location ($x = 12$, just downstream of the obstacle) are shown in Figs. 4a and 4b, respectively. In both figures, the DSGSM gives a significant improvement over the Smagorinsky model in the reversed flow-region ($y \leq 0.75$).

Profiles of averaged turbulent fluctuations in the streamwise (u'^2), normal (v'^2), and spanwise (w'^2) directions at selected streamwise locations are presented in Figs. 5a–5c, respectively. It should be noted that the LES results represent only the fluctuations in the resolved (grid-scale) velocity field. The subgrid-scale contribution is small at this low Re. The dynamic model gives an improvement for u'^2 and v'^2, but not for w'^2.

Figure 6 shows profiles of $C_s(x, y)$ at three different streamwise locations ($x = 10.8$, 12, and 15). Obviously, C_s depends on the grid used and the type of averaging in space and time. There is a sharp gradient near $y = 1$ where the control volumes are densely clustered to resolve the flow above the obstacle. Without an arbitrary damping function, C_s vanishes at the walls and even takes some small negative values near the upper wall.

C. Instantaneous Flowfield

1. Reversed Flow Regions

Figure 7 shows a perspective view of the computational domain near the obstacle. Reversed-flow regions are represented by marking each point with instantaneous negative u with a dot. Since the solid walls are treated as transparent, the reversed-flow region just behind the obstacle is also shown. The figure exhibits the main flow regions (PSRU, PSRD, and the reversed-flow region on the top surface of the obstacle). The clear region near the rear lower corner of the obstacle demonstrates the presence of a secondary recirculating region (SSRD). In Fig. 8, contours of u are presented at one x-y plane at three different times with a time interval of $\Delta t = 1.61$. For convenience, the time for Fig. 8a is designated as $t = 0$, and subsequent figures will be referred relative to that time. Figures 8a–8c show how unsteady the flow is. Near the mean reattachment point of PSRD (6.8h downstream of the obstacle), u is small and oscillating in sign. Intense unsteady free-

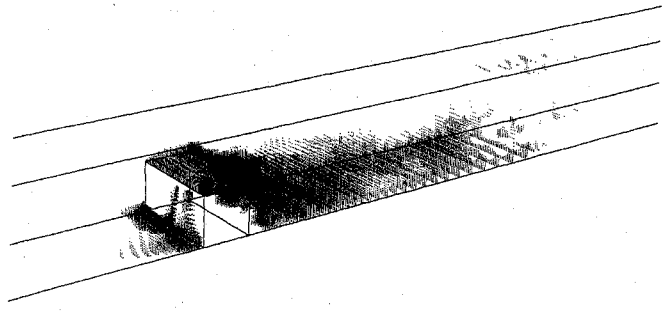

Fig. 7 Regions of instantaneous negative u.

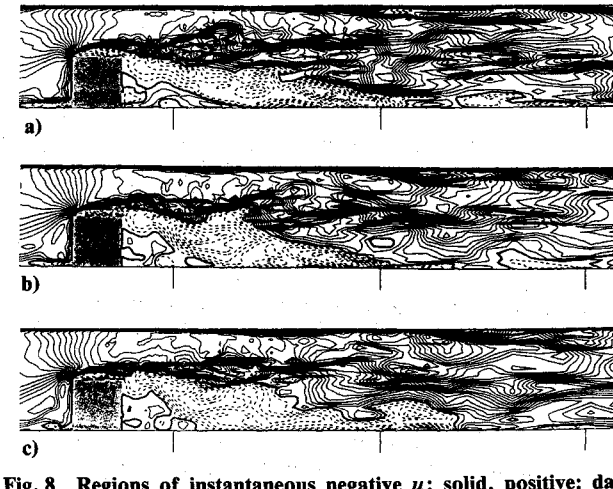

Fig. 8 Regions of instantaneous negative u; solid, positive; dash, negative; thick solid, 0; increment, 0.016: a) $t = 0$; b) $t = \Delta t$; and c) $t = 2\Delta t$.

shear layers formed downstream of the obstacle are noticeable. Intermittent separation on the upper channel wall is observed near the streamwise location of mean reattachment (Fig. 8c). Figures 9a–9c show contours of u at the first grid point away from the lower channel wall at three different times. The instantaneous separation and reattachment lines are far from two dimensional, although the obstacle is geometrically two dimensional. Secondary and tertiary flow regions are present near the obstacle at this Re and are highly unsteady.

2. Pressure Field

In Figs. 10a–10c, we present contours of pressure together with fluctuation-velocity vectors $(u_i - U_i)$ on one x-y plane at three different times. Only the region near the upper right corner of the obstacle is magnified for clarity. Low-pressure regions below a threshold value are represented in grey. The low-pressure regions indicate the location of vortex cores.[9] The vortex formed just above the obstacle is intensified as it travels downstream. Vortex merging/splitting occurs in a quite different manner from that of unbounded free-shear layers. By looking at further snapshots and a video of this flow, we observed that grey regions are intensified initially, become more diffuse downstream, and completely disappear approximately $6h$ or $7h$ downstream of the obstacle. Figures 11a–11d show contours of pressure at four x-y planes, each one-quarter of the spanwise domain size apart. The vortex structures marked by the low-pressure regions are slightly tilted in the x direction but cover approximately 75% of the spanwise dimension. The pressure distribution in the contraction region is almost completely two dimensional.

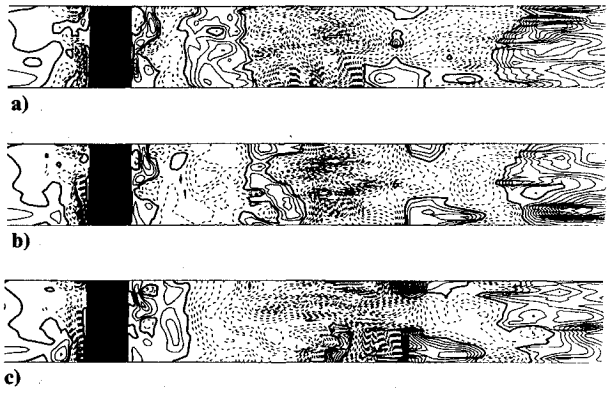

Fig. 9 Regions of instantaneous negative u; solid, positive; dash, negative; thick solid, 0; increment, 0.016: a) $t=0$; b) $t=\Delta t$; and c) $t=2\Delta t$.

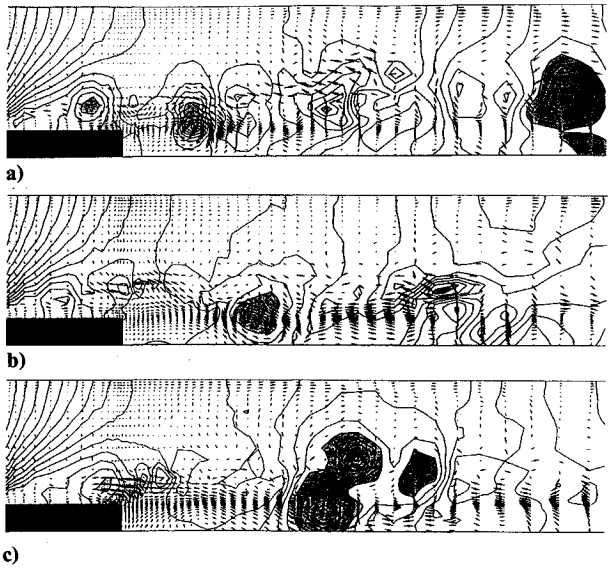

Fig. 10 Contours of pressure along with fluctuation-velocity vectors; pressure increment, 0.096: a) $t=0$; b) $t=\Delta t$; and c) $t=2\Delta t$.

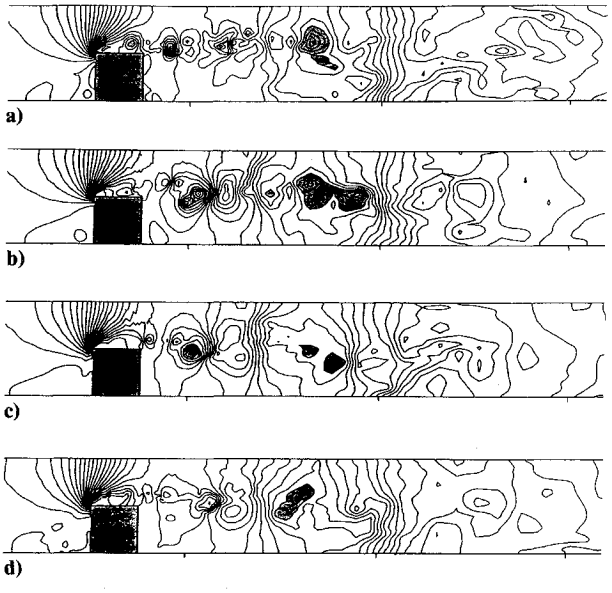

Fig. 11 Contours of pressure; pressure increment, 0.096: a) $z=0.5h$; b) $z=h$; c) $z=1.5h$; and d) $z=2.0h$.

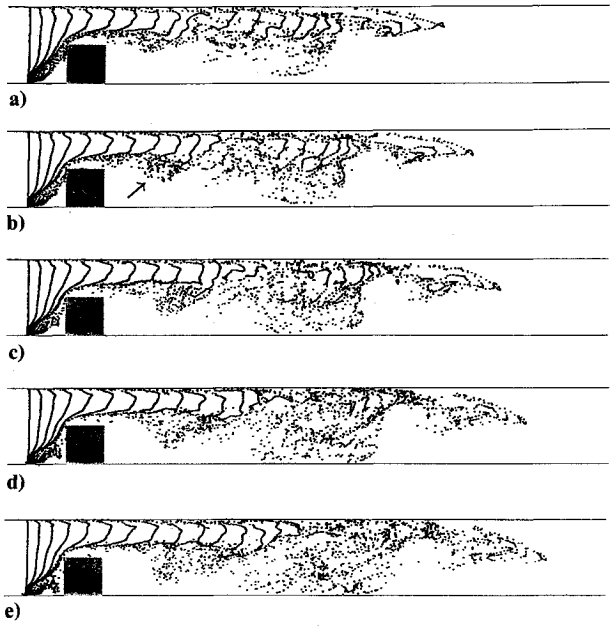

Fig. 12 Simulation with passive particles: a) $t=0$; b) $t=0.5\Delta t$; c) $t=\Delta t$; d) $t=1.5\Delta t$; and e) $t=2\Delta t$.

3. Simulations with Passive Particles

Hydrogen bubbles are often used as passive particles in experiments to study flow structures. To simulate this, "numerical" passive particles are released periodically with a time interval of 0.4 at various "wire" locations. Each release consists of 100 particles. The location of each particle is followed using the simulated velocity field and a third-order Runge-Kutta scheme in time. In Fig. 12, particles are released upstream of PSRU. The formation of a distinct vortex, indicated by an arrow, is observed. Very few particles are entrained into the recirculating region above the obstacle. On the other hand, some particles are entrained into PSRU and show the secondary flow structure there. In Fig. 13, particles are released from

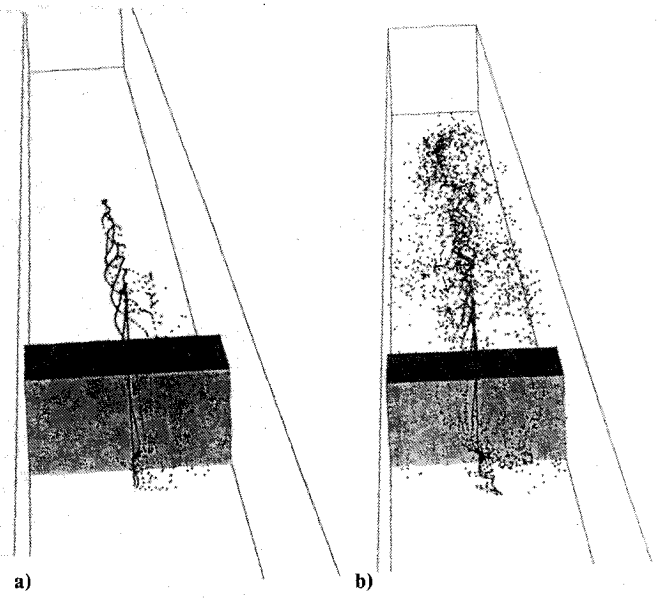

Fig. 13 Simulation with passive particles: a) $t = 1.5\Delta t$; and b) $t = 2\Delta t$.

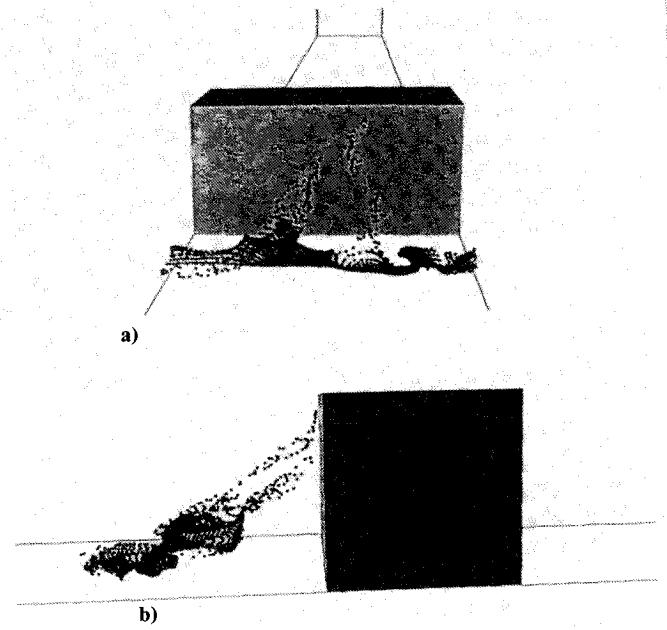

Fig. 14 Simulation with passive particles.

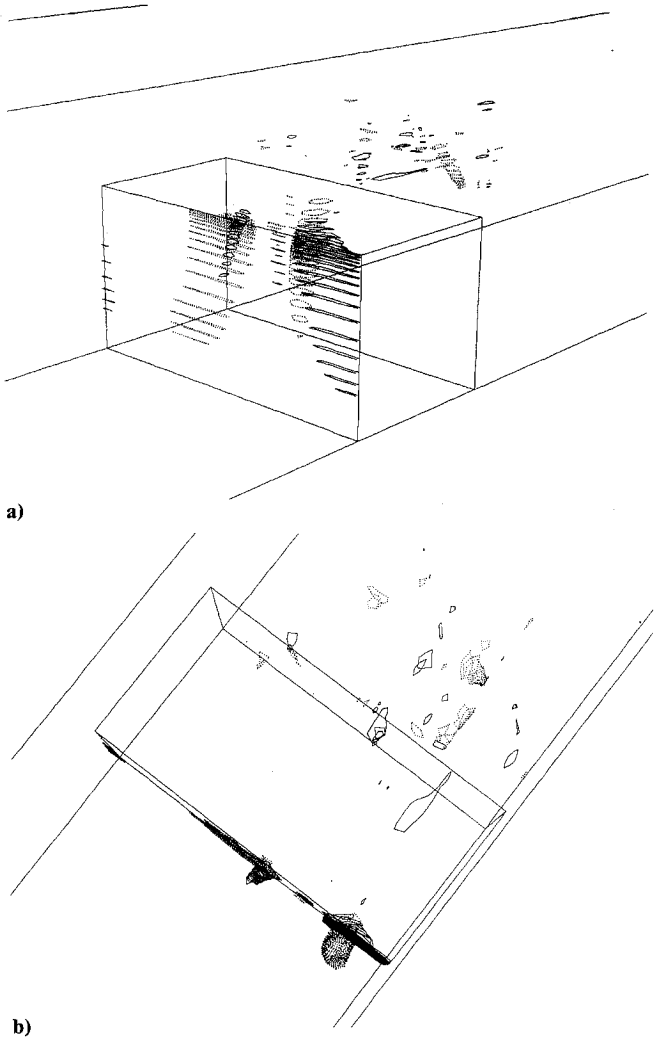

Fig. 15 Contours of ω_y; solid, -9.29; dash, 9.29: a) perspective view; and b) top view.

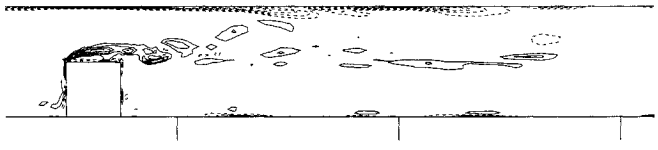

Fig. 16 Contours of ω_z: solid, negative; dash, positive; increment, 3.10.

a vertical "bubble wire" $0.5h$ upstream of the obstacle. In Fig. 13a, particles display streamwise swirling motions, indicating presence of a streamwise vortical structure. Later, particles are diffused in the z direction, and it is hard to discern coherent structure (Fig. 13b). In Fig. 14, particles are released from a horizontal bubble wire h upstream of the obstacle and $0.1h$ away from the lower channel wall. Figures 14a and 14b are at the same time but from different viewpoints. Particles mark a pair of counter-rotating vortices going over the top of PSRU.

4. Contours of Vorticity

Figure 15 shows contours of positive and negative normal vorticity ω_y of the same magnitude at one instant. Figure 15a indicates that a pair of counter-rotating normal vortices develop near the front vertical wall. This is consistent with the particle simulation shown in Fig. 14. The elongated pair is the secondary vortices that are required to satisfy the no-slip boundary condition. To verify this, Fig.15b shows a top view of the same vorticity. These vortices are apparently intensified by vortex stretching due to the strain in the narrowing flow passage. PSRU can be considered an effective "envelope" for the passage. Similar vortices were observed in the experiment of Dimaczek et al.[3] Figure 16 shows instantaneous contours of spanwise vorticity ω_z in a single x-y plane at the same instant. Strong spanwise vortices are shed from the front upper corner of the obstacle and advected downstream. They soon break down into smaller scale structures. All of this structure is much cleaner in a video made by the authors.

V. Summary

A large-eddy simulation of low-Reynolds-number turbulent flow in a channel with a two-dimensional rib on one wall was presented with the wall layers fully resolved. The subgrid-scale model coefficient was computed dynamically. The results obtained were compared with a DNS and showed that the dynamic model yields better results than conventional LES with a fixed model constant. This demonstrates the value of the dynamic subgrid-scale model for computing complex flows.

Application to high Reynolds number flows is currently under investigation.

Acknowledgments

The authors gratefully acknowledge contributions from the following organizations. Financial support for the investigators was provided through the Office of Naval Research Grant N00014-89J-1343 and the Stanford-NASA Center for Turbulence Research. The NASA Ames Research Center provided the computer time for this research.

References

[1]Tropea, C., and Gackstatter, R., "The Flow over Two-Dimensional Surface-Mounted Obstacles at Low Reynolds Numbers," *Journal of Fluids Engineering,* Vol. 107, Dec. 1985, pp. 489–494.

[2]Werner, H., and Wengle, H., "Large-Eddy Simulation of Turbulent Flow over a Square Rib in a Channel," The 7th Symposium on Turbulent Shear Flows, Stanford Univ., Stanford, CA, Aug. 21–23, 1989.

[3]Dimaczek, G., Kessler, R., Martinuzzi, R., and Tropea, C., "The Flow over Two-Dimensional, Surface-Mounted Obstacles at High Reynolds Numbers," The 7th Symposium on Turbulent Shear Flows, Stanford Univ., Stanford, CA, Aug. 21–23, 1989.

[4]Germano, M., Piomelli, U., Moin, P., and Cabot, W., "A Dynamic Subgrid-Scale Eddy Viscosity Model," Summer Program, Center for Turbulence Research, Stanford Univ., Stanford, CA, 1990.

[5]Shaanan, S., Ferziger, J., and Reynolds, W., "Numerical Simulation of Turbulence in the Presence of Shear," Thermosciences Division, Dept. of Mechanical Engineering, Stanford Univ., Report TF-6, Stanford, CA, 1975.

[6]Smagorinsky, J., "General Circulation Experiments with the Primitive Equations, I. The Basic Experiment," *Monthly Weather Review,* Vol. 91, No. 3, 1963, pp. 99–164.

[7]Lilly, D. K., "A Proposed Modification of the Germano Subgrid-Scale Closure Method," *Physics of Fluids A,* Vol. 4, No. 3, 1992, pp. 633–635.

[8]Kim, J., and Moin, P., "Application of a Fractional-Step Method to Incompressible Navier-Stokes Equations," *Journal of Computational Physics,* Vol. 59, No. 2, 1985, pp. 308–323.

[9]Robinson, S. K., Kline, S. J., and Spalart, P. R., "Spatial Character and Time Evolution of Coherent Structures in a Numerically Simulated Boundary Layer," AIAA Paper 88-3577, 1988.